Journal of Industrial and Engineering Chemistry 81 (2020) 228–236

Contents lists available at ScienceDirect

Journal of Industrial and Engineering Chemistry

journal homepage: www.elsevier.com/locate/jiec

Synthesis of PANi nanoarrays anchored on 2D BiOCl nanoplates for photodegradation of Congo Red in visible light region

Abdolhamid Namdarian[a], Amin Goljanian Tabrizi[a], Nasser Arsalani[a,*], Alireza Khataee[b,c,d], Abdolkhaled Mohammadi[a]

[a] Research Laboratory of Polymer, Department of Organic and Biochemistry, Faculty of Chemistry, University of Tabriz, 51666-16471, Tabriz, Iran
[b] Research Laboratory of Advanced Water and Wastewater Treatment Processes, Department of Applied Chemistry, Faculty of Chemistry, University of Tabriz, 51666-16471, Tabriz, Iran
[c] Health Promotion Research Center, Iran University of Medical Sciences, 1449614535, Tehran, Iran
[d] Department of Environmental Engineering, Gebze Technical University, 41400 Gebze, Turkey

ARTICLE INFO

Article history:
Received 11 February 2019
Received in revised form 25 August 2019
Accepted 9 September 2019
Available online 13 September 2019

Keywords:
BiOCl
Polyaniline
Photocatalyst
Visible light
Congo red
Decolorization

ABSTRACT

Photocatalytic processes have attained considerable attention of late years, especially for environmental remediation. Despite extensive research in this area, the need for safer, more efficient, and cost-effective processes has encouraged researchers to develop novel photocatalysis. However, the low active surface area and narrow bandgap limit their photocatalytic performances. In the present research, the 2D BiOCl sheets were successfully synthesized by a new hydrothermal method and decorated by PANi nanoarrays through in-situ oxidative polymerization of aniline. The UV–vis diffuse-reflectance and photo-luminescence spectroscopy revealed the synergistic effects between PANi nanoarrays and 2D BiOCl by enhancing the absorption in the visible light region and reduction of bandgap down to 2.9 eV. Furthermore, the morphology analysis showed the proper decoration of PANi nanoarrays on 2D BiOCl nanoplates. The synthesized nanocomposite with different weight loadings of PANi was taken to evaluate the decolorization efficiency of it. The result exhibited an optimum value of 88.35% at 60 min irradiation under visible light in the photodegradation of Congo Red (CR). Moreover, the probable photocatalytic mechanism for degradation of CR by PANi/BiCOl photocatalyst was proposed based on the scavenger experiments. The outcomes indicated that the PANi promoted the absorption intensity of the pure BiOCl in the visible region. To that, the well-arranged array and considerably high specific surface area of PANi could encourage the transfer of electrons witch generated by the photo to 2D BiOCl substrate and repel the recombination of electron-hole pairs.

Introduction

Environmental pollution with natural contaminants such as antibiotics, organic dyes, and pesticides has become a challenging task due to their carcinogenic and toxic effects on human and organisms [1–3]. Because of increasing daily usage of Congo Red (CR) in different industries including textile, printing, leather, paper, pulp, and cosmetic, remediation of the colored effluents is regarded as a solution to these environmental problems [4]. The mutagenic nature of these effluents impedes their treatment by physical and biological approaches [5]. Degradation of naphthalene and benzene rings of CR cannot apply with ordinary methods. Moreover, because of its aromatic structure, CR possesses high physiochemical, thermal, and optical stability [6].

Various techniques like biodegradation [7], adsorption [8,9], ozonation, photocatalytic degradation, physiochemical treatment, catalytic reduction, and coagulation/flocculation are reported for treatment of dyes [10]. Advanced oxidation processes (AOPs) have drawn considerable attention in recent decades and be more useful for the oxidation of organic pollutants [11]. Despite the economic effectiveness of several adsorbents over CR removal, CR is not degraded by adsorbents and just transferred from liquid phase to solid phase. Therefore, the implementation of AOPs and among them light-driven photocatalytic processes for its high energy and environmental efficiency [12].

Nowadays, tremendous researches have focused on the design and development of innovative, efficient, and cost-effective approaches for remediation of wastewaters [13]. Because of the light-driven photocatalytic system is activated at the visible region

* Corresponding author.
E-mail address: arsalani@tabrizu.ac.ir (N. Arsalani).

https://doi.org/10.1016/j.jiec.2019.09.012
1226-086X/

(can be sunlight at large scales) and no additional reagent or chemical added to the CR solution, make it a great choice for degradation of this pollutant. Recently, bismuth-based compounds, specially BiOX (X = Cl, Br, I) have been received great attention in photocatalytic degradation of water pollutants [14,15]. As a key V–VI–VII ternary semiconductor compounds, all BiOX have a tetragonal PbFCl-type structure, a layered structure described by $[Bi_2O_2]$ sheets inserted by double sheets of halogen atoms [16]. The high photocatalytic activities of BiOX were mostly related to the indirect optical transition and their open crystalline structures. The first one means that the excited electron has to trip a certain distance emitted to the valence band (VB), which decreases the recombination likelihood of the excited electron and hole [17]. Several researchers have reported that nanostructured BiOCl compared to TiO_2 displays the higher photocatalytic degradation performance under irradiation of visible light [18–20]. Furthermore, some dye molecules, including Rhodamine B can easily adsorb on the BiOCl surface, and under irradiation of visible light can be further degraded due to the dye sensitization phenomenon [21]. On the other hand, due to the determining role of morphology and the size of BiOCl particles on its photocatalytic performance, many approaches have been investigated for the synthesis of BiOCl with various morphologies such as solvothermal [22], precipitation [23], the reverse microemulsion route [24], the molecular precursor route [25], calcination [26], microwave irradiation [27], and hydrolysis [21]. Besides its significant photocatalytic activity, the overall photocatalytic efficiency of BiOCl still needs to be improved. In this regard, some modification approaches have been used, including co-catalyst use [28,29], doping [30,31], coupling [32], sensitization [33], graphene use [34], and making defects [35,36]. Also, the conductive polymers including π-conjugated electron systems including polyaniline (PANi), polythiophene, polypyrrole, and their derivatives indicated the great encouraging in photocatalytic processes thanks to their attractive features including broad absorption in the visible light region and excellent stability [37,38]. Besides, PANi is relatively cheap with simple synthesis approach in comparison with doped noble metals. Some reports depict the mixture of conductive polymers and some semiconductors to advance their photocatalytic performance as sensitization agents. Wang et al. [39] have reported the modification of BiOCl by PANi via chemisorption approach. The obtained PANi/BiOCl photocatalyst declared many plates of BiOCl with anchored PANi particles on their surface. The main morphological difference between the nanocomposites synthesized here with the earlier one reported by Wang by al. one is the creation of PANi nanoarrays by in-situ polymerization approach compared to nanoparticles of PANi attached on the surface of BiOCl sheets via chemisorption method. Therefore, we can consider the improvement in synthesis approach and morphological features of PANi/BiOCl to its enhanced performance. In another study, a multifunctional $Ni_{0.5}Zn_{0.5}Fe_2O_4$@PANi modified BiOCl was developed by Tanwar et al. [40] as highly effective and visible light-driven photocatalyst in the degradation of four toxic dyes. In that composite, the ferrite and PANi components absorb photons to create electron-hole pairs. This group in another work [41] prepared PANi/Fe^0 doped BiOCl by chemisorption of PANi/Fe^0 fibers on BiOCl plates. The nanocomposite showed 1.62 eV decrease in the estimated bandgap value compared to pure BiOCl with improved photocatalytic performance in the removal of CR under irradiation of visible light. However, in prior works, morphology control of PANi on BiOCl substrate has not been addressed, which may reduce the synergistic effects of two components. Hence, the construction of specially structured composites of BiOCl and PANi, which allows highly efficient utilization of PANi, remains a challenge.

In the present work, as shown in Scheme 1, we employed a novel two-step approach for the fabrication of PANi/BiOCl photocatalyst. For this means, firstly, 2D BiOCl sheets were synthesized by a hydrothermal approach then the in-situ oxidative polymerization of aniline monomer was performed in the existence of them to create PANi nanoarrays on their surface. The obtained PANi/BiOCl nanocomposite showed well-arranged nanoarrays of PANi on 2D BiOCl sheets surface and showed remarkable photocatalytic activity compared to previously reported work [39] in the degradation of CR under visible light irradiation.

Experimental

Materials

The bismuth(III) nitrate pentahydrate ($Bi(NO_3)_3.5H_2O$), sodium chloride (NaCl), ammonium persulfate ($(NH_4)_2S_2O_8$), hydrochloric acid (HCl), aniline ($C_6H_5NH_2$), ethanol (C_2H_5OH), and KCl were all in analytical grade and purchased from Merck. The reagents were utilized as received without further purification. The distilled and deionized water was used during experiments.

Synthesis of 2D BiOCl sheets

The 2D BiOCl layers were synthesized as described elsewhere [42]. In brief, 1.94 g $Bi(NO_3)_3{\cdot}5\ H_2O$ was dissolved in 100 mL distilled water through ultrasonic treatment. Then, under stirring for 15 min, 20 mL of saturated NaCl solution was added into the above mixture. The solution was then moved into a Teflon-lined stainless autoclave. Then the autoclave was heated at 150 °C in an oven for four hours and then cooled down to room temperature naturally. The obtained precipitate was gathered by centrifugation and to remove the residual ions; it was washed with EtOH and DI water. The 2D BiOCl sheets were then dried at 30 °C for further use.

Synthesis of 2D BiOCl decorated by PANi nanoarrays

In-situ oxidative polymerization of aniline monomer by APS in the existence of 2D BiOCl sheets was used to create different weight loadings of PANi nanoarrays on the surface of 2D BiOCl sheets as substrate. As an example, for the preparation of PANi/

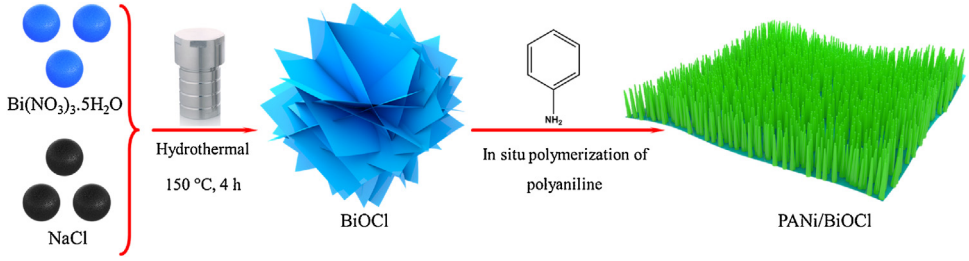

Scheme 1. Schematic of the formation of PANi/BiOCl nanocomposite.

BiOCl 5%, a solution containing 32.64 mg APS in 5.23 mL distilled water and 0.70 mL HCl was firstly prepared and stored in the refrigerator as solution A. Then, 1.55 mL HCl and 1.44 mL ethanol were added to 13 mL distilled water in the ice bath. After that, 19.35 μL aniline monomer (0.21 mmol) was added to the above solution and agitated for 15 min. Subsequently, 600 mg of BiOCl was added and mixed by a stirrer to obtain BiOCl contained solution (solution B). Finally, solution A was added to solution B and stirred by 18 h for in-situ oxidative polymerization of aniline monomer on 2D BiOCl sheets. The final precipitate was rinsed by water and EtOH then dried at 60 °C. For the preparation of different nominal weight loadings of PANi, corresponding initial values of aniline monomer were calculated and used in each sample preparation. The amount of BiOCl, 600 mg, was constant for all of the specimens.

Characterization

A Siemens D-500 Diffractometer with Cu K_α radiation (wavelength, λ = 1.5406 °A) was employed to define the crystal structures of specimens over a 2θ range from 10° to 70° (Siemens AG, Germany). The surface structural sates of examples before and after PANi growth were acquired by Raman spectroscopy (Bruker, Germany). Fourier Transform Infrared Spectroscopy (FT-IR) of the samples were recorded on Bruker Optics TENSOR 27 spectrometer using KBr pellets. Surface morphology imaging was carried out on field-emission scanning electron microscopy (FE-SEM MIRA3 FEG-SEM, Tescan, Czech) and a transmission electron microscopy on JEOL 2100F (JEOL Ltd, Japan). The specific surface area was obtained by Belsorp Mini II (Japan). The UV–vis diffuse-reflectance spectra were calculated using a Varian Cary 5000 spectrophotometer (Agilent, Canada). An Agilent 6890 gas chromatograph with a 30-m to 0.25-mm HP-5MS capillary column coupled with an Agilent 5973 mass spectrometer (Canada) was used to identify the intermediates generated during the CR degradation process. Thermogravimetric studies were performed by TG209F1 (Netzsch Instrument Crop., Germany). Photoluminescence (PL) spectra were acquired on a fluorescence spectrophotometer (Varian, United States of America). The flat band potential (V_{fb}) of semiconductor particle films was measured by Mott–Schottky method in (1 mol L^{-1} KCl solution, pH 6.8, frequency of 1 kHz, and without the Xe lamp irradiation) which is carried out in conventional three-electrode cells using a CHI660D electrochemical workstation (shanghai Chenhua Instrument Co., Ltd., Shanghai, China). The UV–vis spectrophotometer (Shimadzu UV2800, Japan) was employed to optical absorbance of CR solutions in calculating the photocatalytic activity of photocatalysts.

Photocatalytic activity test

The photocatalytic performance of the PANi/BiOCl nanocomposites was assessed on CR photodegradation by a 225 W Xe light with a 400 nm cut off filter as a visible-light simulator. The spectral range of presentation 400–1000 nm. The distance between the solution and the lamp was 15 cm and the facula diameter was 5 cm. In each experiment, 5 mg nanocomposite sample was added to 50 mL CR solution at room temperature. After that, to formation the completing of an adsorption–desorption balance, the suspension was agitated in the dark for 1 h. Then, for 1 h, the solution was irradiated by visible light under magnetic stirring. At each interval, 3 ml of the suspension was gathered by a syringe and then to remove the photocatalyst the slurry sample was centrifuged (10,000 rpm, 10 min). Therefore, the concentration of CR was analyzed at 499 nm by a spectrophotometer. To compare the photocatalytic activities of the PANi/BiOCl, the photocatalytic degradation over BiOCl micro-sheets and PANi micro-fibers were also performed under the same conditions. The decolorization efficiency (*DE*, %) of CR solution by photocatalyst at time *t* was calculated using Eq. (1):

$$DE(\%) = \frac{C_0 - C}{C_0} \times 100 \quad (1)$$

where, C_0 and C (mg L^{-1}) are the concentration of CR at t = 0 and at time t (min), respectively.

For identification of produced intermediates in photodegradation of CR, after 45 min of the photocatalytic process, the composite was eliminated, and then the solution of treated CR was filtered. Afterward, the solution was extracted by diethyl ether

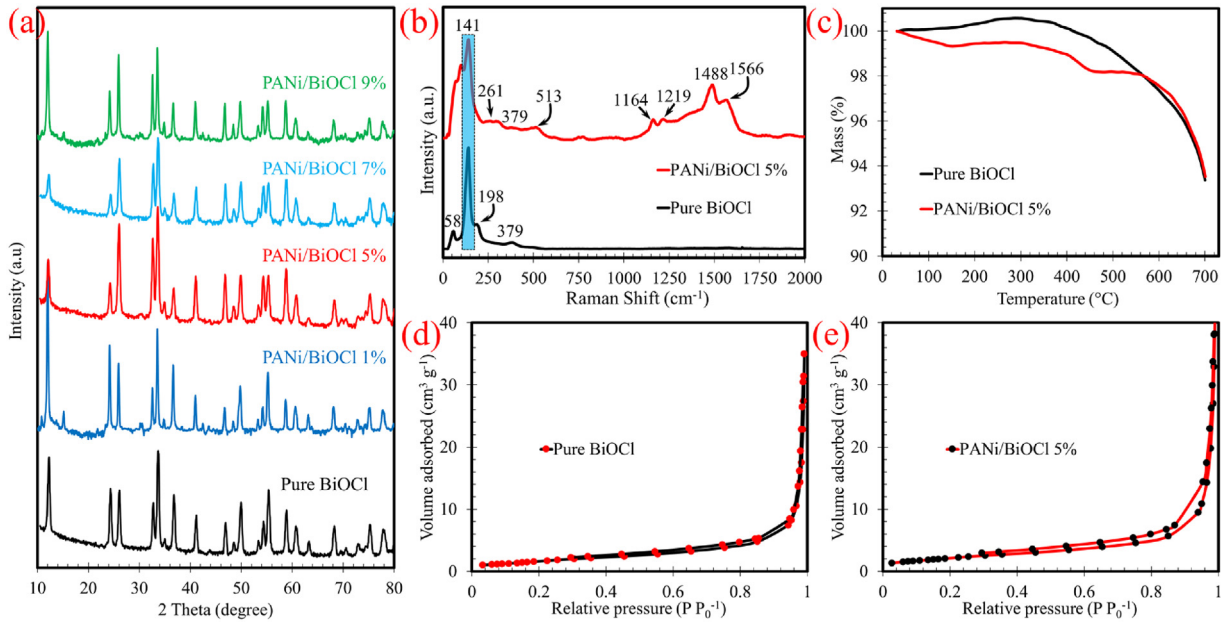

Fig. 1. (a) XRD patterns of the BiOCl, PANi/BiOCl nanocomposites containing from 1, 5, 7, and 9 wt% PANi (b) Raman spectrum (c) TGA curves and (d, e) Nitrogen adsorption–desorption isotherm of pure BiOCl and 5 wt% PANi/BiOCl nanocomposite.

three times. Subsequently drying up of diethyl ether, *N,O*-bis-(trimethylsilyl)-acetamide was added in 60 °C for 30 min as derivative. The obtained sample was then analyzed by GC–MS [43].

Results and discussion

Characterization of PANi/BiOCl photocatalysts

Fig. 1a indicates the XRD patterns of BiOCl and a set of PANi/BiOCl photocatalysts with 1, 5, 7, and 9 wt% of PANi. The XRD pattern of hydrothermally synthesized BiOCl is inconsistent with standard tetragonal structure (JCPDS 01-073-2060). The key diffraction peaks appear at 2θ's of 11.98°, 24.10°, 25.40°, 33.45°, 34.40°, 36.50°, 41.51°, 46.52°, 49.6°, 55.70°, 58.41°, 61.33°, 75.43°, and 77.32° which correspond to the (0 0 1), (0 0 2), (1 0 1), (1 1 0), (1 1 1), (0 0 3), (1 1 2), (2 0 0), (1 1 3), (1 0 4), (2 1 2), (1 1 4), (2 1 4), and (3 1 0) crystal planes of BiOCl, respectively. Furthermore, based on the XRD results, the crystal lattice factors of pure BiOCl were calculated as a = b = 0.3891 °A, c = 0.7369 °A, which were under the literature [44]. There are not considering changes in peak positions and shapes for PANi/BiOCl specimens compared to BiOCl, signifying that the lattice structure of BiOCl was not affected during modification by PANi. The main difference is that the peak intensities of the BiOCl reduced upon the increasing of PANi content, which could be attributed to the reduced penetration depth of the X-rays due to the deposition of PANi layer. Moreover, a considerable reduction in peak ratio of (0 0 1) over (1 1 0) for nanocomposites compared to BiOCl is observed which indicates that in nanocomposite the PANi arrays grow favorably along the [0 0 1] orientation with [0 0 1] facets as the main surface [45], the phenomenon which further confirmed by the HRTEM images in the following.

The Raman spectroscopy was utilized to additionally examine the surface structural sites before and after PANi nanoarrays formation on BiOCl sheets. Based on Fig. 1b, four peaks are located at 58 cm^{-1}, 141 cm^{-1}, 198 cm^{-1}, and 379 cm^{-1} for BiOCl sheets. The former peak is allocated to the surface or interface stretching modes of BiOCl. The next two peaks are respectively belonging to A_{1g} and E_g inherent Bi–Cl stretching mode in BiOCl. The final peak is associated with B_{1g} and E_g band which initiates from the motion of O atoms [46]. In the case of 5 wt% PANi/BiOCl nanocomposite (PANi in emeraldine salt form), due to surface changes of BiOCl substrates, the peaks at 58 cm^{-1} and 198.2 cm^{-1} are almost disappeared. Moreover, some peaks related to PANi were appeared such as the C—H bending of quinoid ring at 1164 cm^{-1}, the C—H bending of the benzenoid ring at 1219 cm^{-1}, and vibrational mode of the quinonoid unit at 1488 and vibrational mode of the benzenoid unit at 1566 cm^{-1} [47–49], which show the successful formation of PANi nanoarrays on BiOCl sheets.

Fig. 1c shows the TGA graphs of pure BiOCl and 5 wt% PANi/BiOCl nanocomposite scanned from 20 °C to 700 °C under an air atmosphere with an increasing rate of 20 °C min^{-1}. The high stability of BiOCl in the working atmosphere is clear from negligible weight loss in TGA. The insignificant weight loss before 150 °C is mainly due to the vaporization of physically adsorbed water and in the second step, during 200 °C thermal degradation of the low weight oligomers is causes weight loss [50]. The downward trend after 600 °C in this curve is related to the decomposition of BiOCl structure [51]. On the other hand, from the decomposition curve of the nanocomposite, it can be observed that a continuous low rate weight loss starts at about 50 °C up to 400 °C. The former (about 1%) is caused by the evaporation of trapped moisture in the matrix of the nanocomposite, as described for BiOCl [48] and the latter (about 2%) is as a result of the complete thermal degradation of polyaniline chains. The thermal decomposition after 600 °C is related to the BiOCl content of nanocomposite.

The active surface area of a catalyst plays a significant role in catalytic activity by enhancing the number of active sites for catalytic reactions. By the creation of nanoarrays of PANi on the sheets of BiOCl, it is expected that the active surface area and pore volume to be increased [52]. So nitrogen adsorption–desorption was utilized to measure the specific surface area and pore size distribution of the prepared photocatalysts. Fig. 1d and e display the results for bare BiOCl and 5 wt% PANi/BiOCl nanocomposite. These isotherms are related to the type-IV isotherms demonstrating the mesoporous structure of the samples [53,54]. The BET surface area and pore volume of the composite are 7.80 $m^2 g^{-1}$ and 0.065 $cm^3 g^{-1}$, respectively, which are higher than that of pure BiOCl (6.43 $m^2 g^{-1}$ and 0.052 $cm^3 g^{-1}$). An increased BET surface area of the nanocomposite results from the growth of PANi

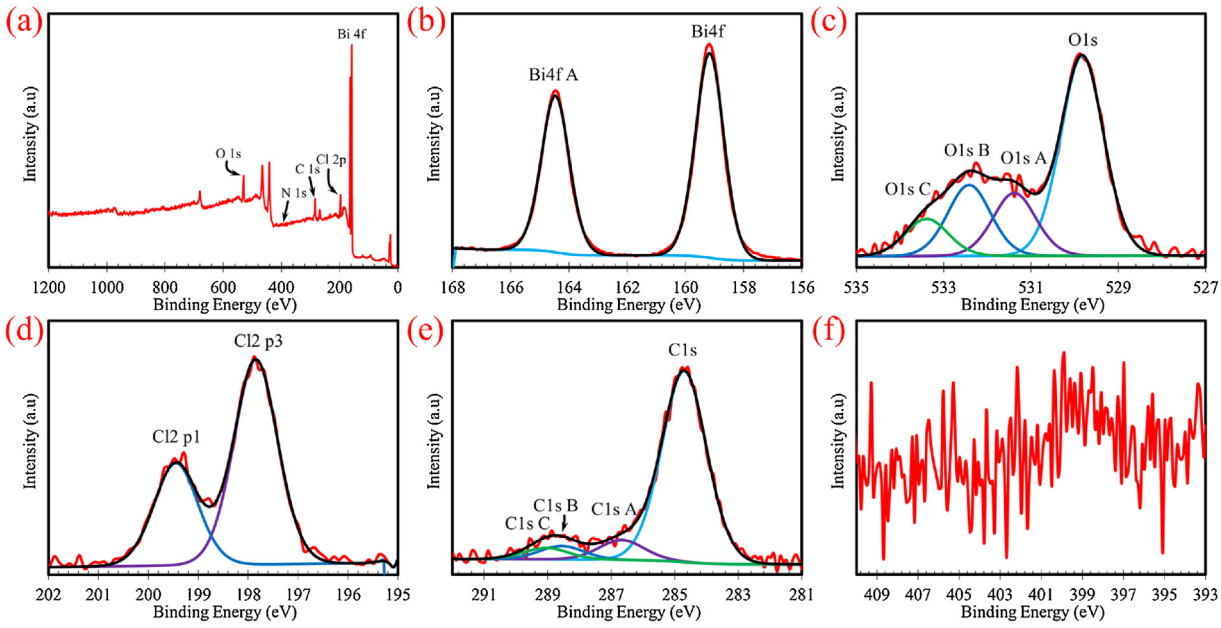

Fig. 2. XPS spectra of 5 wt% PANi/BiOCl nanocomposite: (a) full survey spectrum, (b) Bi 4f, (c) O 1s, (d) Cl 2p, and (e) C 1S, (f) and N 1S regions.

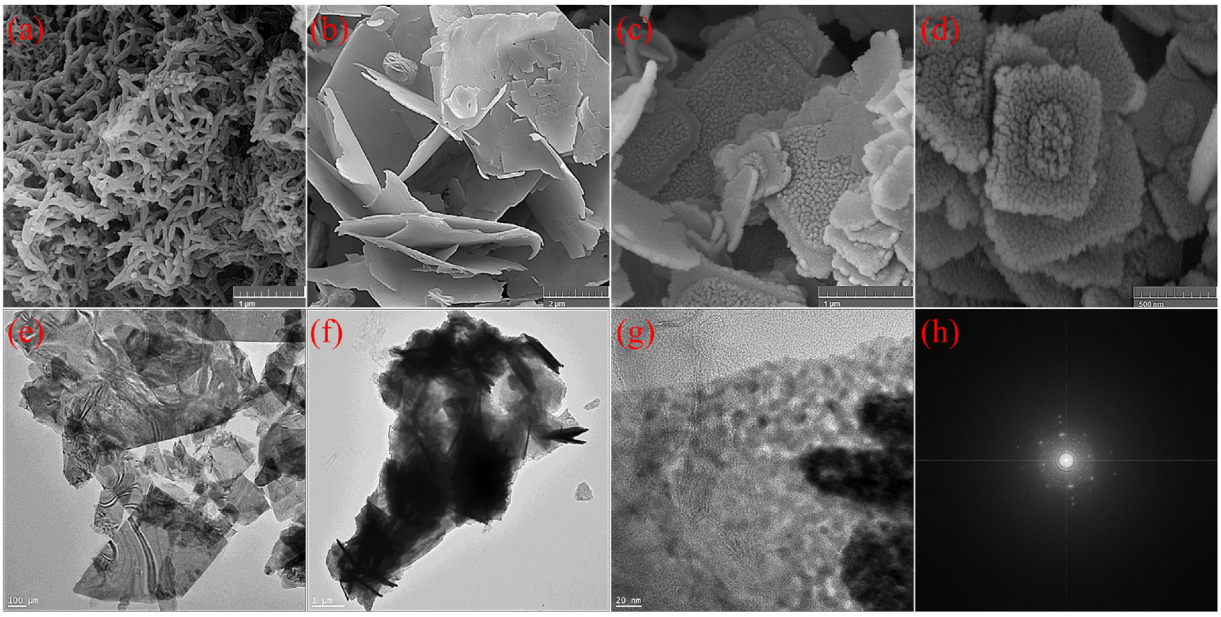

Fig. 3. FESEM images of (a) pure PANi, (b) pure BiOCl, (c, d) 5 wt% PANi/BiOCl nanocomposite, HRTEM images of (e) Pure BiOCl, (f, g) PANi/BiOCl, and (h) SAED pattern of 5 wt% PANi/BiOCl nanocomposite.

nanoarrays which further facilitates charge transportation and enhances the photocatalytic activity of nanocomposite [55].

XPS elucidated the elemental composition and chemical state of the nanocomposite. The resultant XPS spectrum (Fig. 2a) shows that the as-prepared 5 wt% PANi/BiOCl nanocomposite contains Bi, O, Cl, C, N, and S elements. Moreover, an investigation was carried out to elucidate the chemical state of elements in the nanocomposite. In Fig. 2b, two stiff peaks are seen at 159.17 and 164.47 eV, which could be related to Bi $4f_{7/2}$ and Bi $4f_{5/2}$, respectively, representing bismuth exists as Bi^{3+} [56]. The XPS peaks for O1s (Fig. 2c) at a binding energy of 529.84 eV and 531.5 eV are related to oxygen species of a Bi—O bond and −OH, respectively [57,58]. The peaks located at 197.85 eV and 199.45 eV correspond to Cl 2p levels as the Cl $2p_{1/2}$ and Cl $2p_{3/2}$ energy levels (Fig. 2d) [59,60]. In Fig. 2e, the N 1s core spectrum indicates peaks at around 399 eV caused by the quinoid imine (–N–), benzenoid amine(–NH–), and imine ($-NH^+$) groups [61]. Consequently, the XPS analysis also approves the existence of BiOCl and PANi in the nanocomposite.

One of the essential factors to achieve an excellent catalytic performance is having a proper morphology and uniform distribution of components on the surface of the catalyst. Fig. 3 represents the SEM images of the as-prepared PANi (a), BiOCl (b) and 5 wt% PANi/BiOCl (c), respectively. In Fig. 3a, it could be seen clearly that the pure PANi composed of the inter-tangled network of PANi nanofibers and from Fig. 3b, the BiOCl sheets consist of smooth sheets with the thickness of each sheet is almost 50 nm. In Fig. 3c, the 5 wt% PANi/BiOCl mostly included many BiOCl 2D sheets with small fluffy shaped arrays of PANi formed densely on them. A significant difference in morphology was observed here for chemically sensitized PANi/BiOCl nanocomposite, in this work, with that of chemically absorbed PANi nanoparticles on BiOCl microplates which reported previously [39]. The HRTEM image further confirms the sheet-like morphology of the pure BiOCl (Fig. 3e). Also, the HRTEM images for nanocomposite revealed the flaky structure of BiOCl with deposited PANi on its surface (Fig. 3d, e). The darker region in the central parts of sheets shows the higher contents of PANi following FESEM images. As can be seen in Fig. 3f, the SAED represents both the crystalline nature of BiOCl, as bright dots, and amorphous phase of PANi, as scattered halos, which formed on BiOCl sheets [46].

The EDX spectra of 5 wt% PANi/BiOCl composite (Fig. 4a) further confirms its combination of bismuth, oxygen, chlorine, carbon, and nitrogen elements, and signifies the successful loading of PANi on BiOCl.

Fig. 4b indicated the photoluminescence spectra of BiOCl and 5 wt% PANi/BiOCl. Two emission peaks are observed for both BiOCl and nanocomposite at 365 nm and 395 nm. While the forms and peaks positions of 5 wt% PANi/BiOCl are like the pure BiOCl, considerable reduction in peak intensities are observed which clearly show the weak recombination of the electron-hole pairs to boost photon efficiency. Fig. 4c represents the UV–vis diffuse reflectance absorption spectra of the prepared BiOCl and 5 wt% PANi/BiOCl composite in the range of 200–800 nm. As seen, the absorption edge of BiOCl placed at 380 nm, below visible region, indicating BiOCl displays a strong light response in the UV range with low visible light absorption [62]. On the other hand, the DRS absorbance spectrum of nanocomposite shows considerable enhancement in light absorption in the visible range with some enhancement in the UV range, too; thus, the composite can absorb both UV and visible light. The absorption edge for nanocomposite was red-shifted slightly. The observations demonstrate that the sensitized PANi/BiOCl will be certainly activated by visible light. Using the Tauc equation, the bandgaps of the specimens are assessed as the following [63]:

$$\alpha h\vartheta = A(h\vartheta - E_g)^{\frac{n}{2}} \quad (2)$$

where A denotes proportional constant, α is absorption coefficient, E_g represents bandgap, and $h\nu$ is photon energy. With considering n = 4 for an indirect transition in PANi/BiOCl photocatalyst, the intercept of a plot of $(\alpha h\nu)^2$ vs. $h\nu$ yields the bandgap of the photocatalyst, which is 3.1 and 2.9 eV for BiOCl and composite, respectively (Fig. 4d). Also, the UV–vis diffuse reflectance absorption spectra of pure PANi and its bandgap estimation (PANi E_g = 3.09 eV) depicted in the supplementary information (Fig. S1).

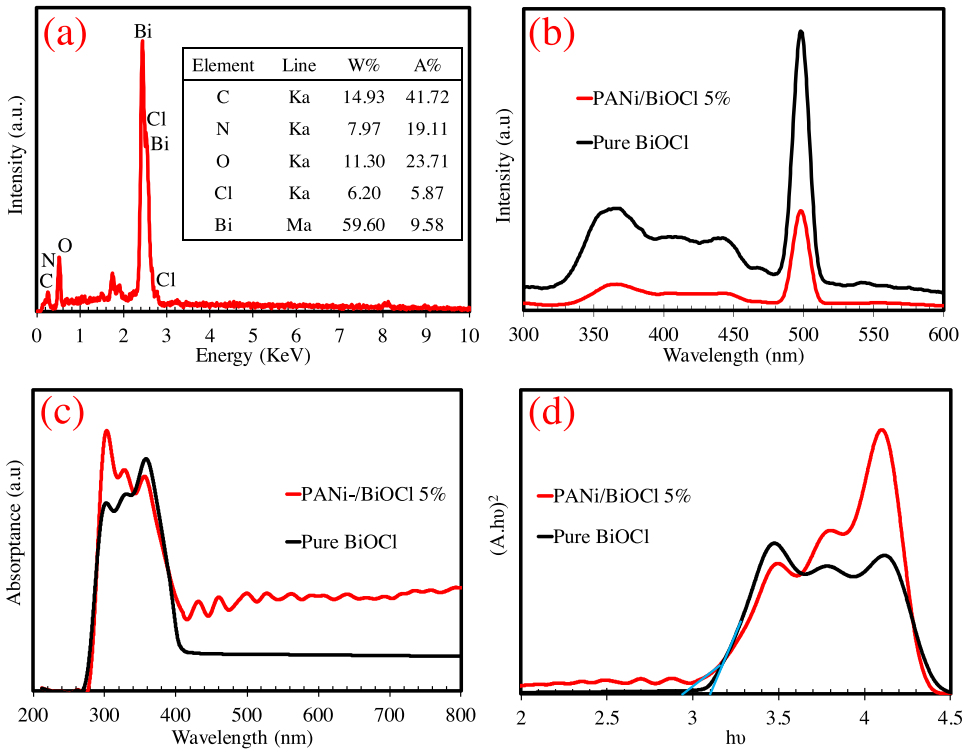

Fig. 4. (a) EDX spectrum for 5 wt% PANi/BiOCl nanocomposite (b) Photoluminescence spectra, (c) UV–vis diffuse reflectance absorption spectra, and (d) tauc plots (n = 4) of $(\alpha h\nu)^2$ vs. photon energy ($h\nu$) of the prepared BiOCl and 5 wt% PANi/BiOCl composite.

The considerable low value of Eg for composite, which is located in the visible range, implies that it could be an efficient photocatalyst under irradiation of the visible light.

Photocatalytic activity

Monitoring the optical behavior of CR at 499 nm upon the excitation of photocatalysts with the visible light simulator was used to assess the photocatalytic activities of the PANi/BiOCl photocatalysts containing different weight percentages of PANi in 1–9 wt% range. As seen in Fig. 5a, after 60 min irradiation, the DE values of 19.20%, 23.76%, 88.35%, 37.26%, and 24.37% for CR solution were obtained for PANi/BiOCl composite with mass ratios of PANi containing 1%, 3%, 5%, 7%, and 9%, respectively. Thus, by increasing the weight percentage of PANi up to 5%, the efficiency of the photocatalyst was improved but at higher loadings, a significant reduction was observed. A comparison was made among the 5 wt% PANi/BiOCl, PANi, and pure BiOCl in

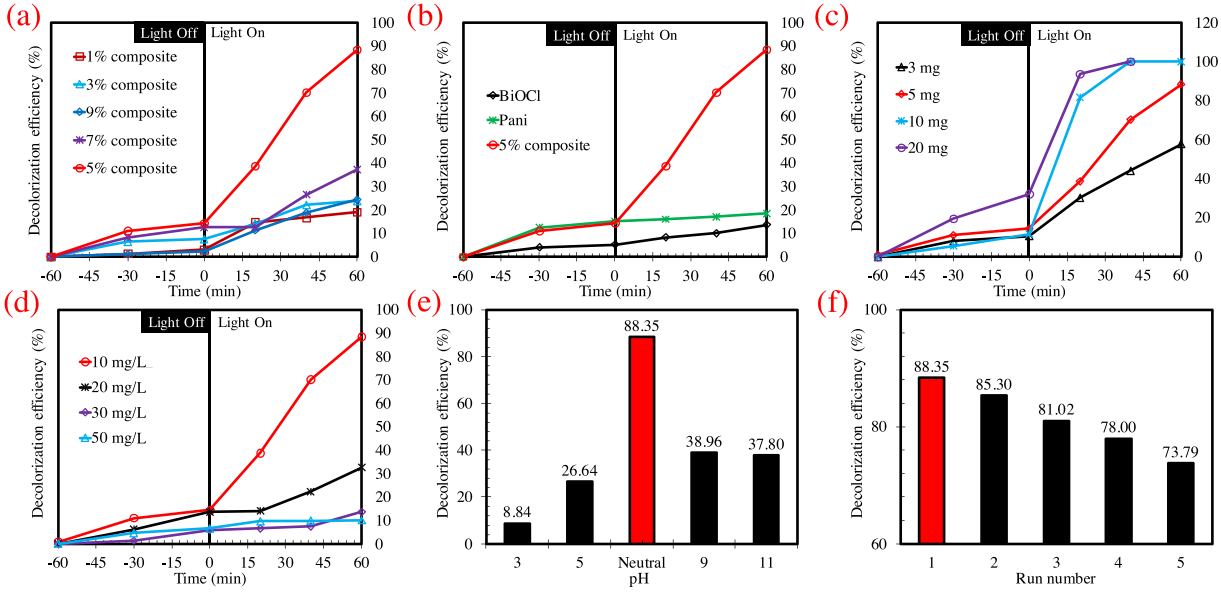

Fig. 5. Decolorization efficiency of Congo red over 10 ppm (a) PANi/BiOCl composites 5 mg with different weight percentages (1, 3, 5, 7, and 9%) under irradiation of visible light (b) pure BiOCl, pure PANi, and 5 wt% PANi/BiOCl nanocomposite; effects of operational conditions including (c) catalyst amount, (d) the concentration of dye, (e) the pH of solution and (f) the effect of run number on decolorization efficiency.

the degradation of CR. As seen in Fig. 5b, the nanocomposite with 88.3% DE has considerable efficiency compared to 13.6% and 18.5% for pure BiOCl and pure PANi, respectively. The 5 wt% PANi/BiOCl photocatalyst shows the highest photodegradation activity and removed almost 88.35% of CR after 60 min irradiation of visible light. The processing time, herein, is lower than the reported value for earlier described PANi/BiOCl composite [39]. The results designate that the presence of PANI nanoarrays boosted the photocatalytic activity of the all composites in compared to the pure BiOCl. It seems that at the higher mass ratios of PANi, it impedes light absorption of BiOCl by totally blocking of its surface. Since by increasing the weight loadings, of PANi below 5 wt%, the photocatalytic activity is enhanced; thus, it shows a synergistic effect between PANi nanoarrays and BiOCl. We believe that the photocatalytic the degradation capability of our developed catalyst is highly analogous and even more enhanced than the previously reported BiOCl modified catalysts [39,41]. For showing the synergistic effect between Vis-light irradiation and PANi/BiOCl composite, the difference between photolysis, adsorption, and photocatalysis was studied. The results were about 7.15%, 19.72%, and 74.60% CR removal under optimum conditions for photolysis, adsorption, and photocatalysis; respectively.

The effect of catalyst amount, dye concentration, and pH of the solution was investigated as operational parameters on DE. Fig. 5c shows the effect of catalyst amount on catalyst performance at pH 7 and dye concentration of 10 mg L^{-1}. As seen, by increasing the catalyst quantity from 3 to up to 20 mg, its performance was improved, but with considering economic viewpoints, the amount of 10 mg was selected as the optimum value. On the other hand, the initial dye concentration also has a significant effect on its performance (Fig. 5d) so that at the higher levels than 30 mg L^{-1}, the DE was decreased; the situation which was attributed to the surface blocking of the active sites of catalyst due to adsorption of dye molecules which impedes the hydroxyl radical formation and subsequently reduces the catalyst performance [64]. A digital photograph of Congo red removal using the prepared 5 wt% PANi/BiOCl provided as Fig. S2 in SI.

Moreover, one of the essential factors in the removal of various dye pollutants is the pH of the solution. The result of the pH was investigated on the photocatalytic degradation of 10 mg L^{-1} CR in the pH range of 3–11. As seen in Fig. 5e, the optimum pH is 7 with a DE value of %88.35. Until now, three mechanisms have been reported for photodegradation of dye molecules: (1) degradation by hydroxyl radicals, (2) oxidative degradation by positive holes on valence band of the photocatalyst, and (3) reductive degradation by electrons on conduction band of the photocatalyst. Furthermore, the adsorption/desorption of dye molecules and the separation of electron/hole pair on the surface of semiconductor are also affected by the pH of the solution. pH_{pzc} indicated that pH at which the electrical charge density on composite surface is equal to zero. pH_{pzc} was determined by the pH drift method [65]. As an anionic an azo dye, the interaction of H^+ ions with the azo bond of CR in an acidic solution reduces its electron densities. Also, the agglomeration of particles occurs, which reduces the photon absorption efficiency of nanoparticles. In contrast, in neutral and alkaline environments, the catalyst surface has a negative charge due to the adsorption of OH^- ions. The pH_{pzc} of 5% PANi/BiOCl is equal to 4.8 by the drift method. Therefore, when pH is below the pH_{pzc}, the photocatalyst particles are protonated and become positively charged. However, when the pH is above the pH_{pzc}, the catalyst particles are deprotonated and become negatively charged. Consequently, the presence of electrostatic attraction between anionic CR dye and the catalyst surface prevents the undesired events occurred in acidic media and thus showed the better performance [66].

To elucidate the nature of active species involved in the degradation process, the scavenger trapping experiments were

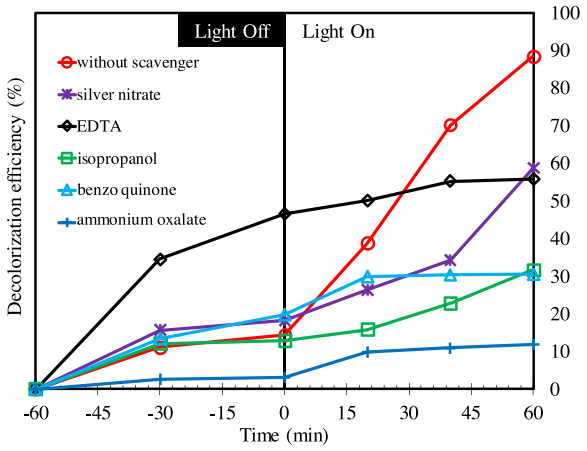

Fig. 6. Photocatalytic decolorization of CR with 5 wt% PANi/BiOCl nanocomposite by adding various scavengers.

conducted. As seen in Fig. 6, due to the addition of $AgNO_3$ (an e^- trapper), 58.65% of CR was degraded after 60 min irradiation compared to 88.35% without scavenger, indicating that the electrons have low effect on the DE. On the other hand, addition of Ethylenediaminetetraacetic acid (EDTA, photo-generated h^+ scavenger), causes the 55.9% degradation of CR, suggesting that the photo-generated holes have low effect on the DE. Likewise, when either isopropanol (IPO, $^{\bullet}OH$ scavenger) or benzoquinone (BQ, $O_2^{\bullet-}$ scavenger) was added into the photoreactor, a significant change in photodegradation activity was not seen this designates that both the $^{\bullet}OH$ and $O_2^{\bullet-}$ may have a meager role in the degradation process. However, it is seen that in the presence of ammonium oxalate (AO, h^+ scavenger), the degradation efficiency was considerably reduced (11.91%) indicating that the holes are the main active agents in the degradation of CR via 5 wt% PANi/BiOCl nanocomposite.

The stability and reusability of the photocatalyst were investigated by repeating the photocatalysis process five times. After five recycles in the photodegradation of CR, 17% loss of activity was observed for BiOCl 5 wt% PANi photocatalyst, and the DE remained above 73%, as shown in Fig. 5f. This slight decrease in the catalyst activity could be described by the loss of structural PANi and/or BiOCl sheets during stirring process or deactivation of a number of active sites over the composite during the CR degrading processes. These results signify the great stability of PANi/BiOCl 5 wt% photocatalyst during the photocatalytic process. Moreover, stability of PANi/BiOCl 5 wt% was studied through various techniques after CR photodegradation.

Fig. 7a represents the SEM images of the 5 wt% PANi/BiOCl after photocatalytic degradation of CR. The stability of PANi arrays on BiOCl was indicated. As shown in Fig. 7b the stability and combination of bismuth, oxygen, chlorine, carbon, and nitrogen elements were confirmed by EDX spectra of 5 wt% PANi/BiOCl composite. For the study of the active surface area of 5 wt% PANi/BiOCl nanocomposite after CR photodegradation, the N_2 adsorption–desorption analysis was performed. Fig. 7c shows the stability of the mesoporous structure of the sample after photocatalysis. The BET surface area and pore volume of the composite are 7.03 $m^2 g^{-1}$ and 0.061 $cm^3 g^{-1}$, respectively.

Finally, the stability of surface functional groups was studied through FT-IR technique. Fig. 7d shows the FT-IR spectra of 5 wt% PANi/BiOCl before and after photocatalysis. The strong peak at low frequency (about 525 cm^{-1}) for BiOCl is attributed to the vibration of Bi—O bonds. Characteristic absorption bands at 1554 cm^{-1}, 1378 cm^{-1}, 1298 cm^{-1} corresponding to stretching vibration for C=C in the quinoid unit, C=C is stretching vibration for the benzenoid group, and C–N stretching mode of the benzenoid unit, respectively [67]. For the FT-IR spectra of 5 wt% PANi/BiOCl

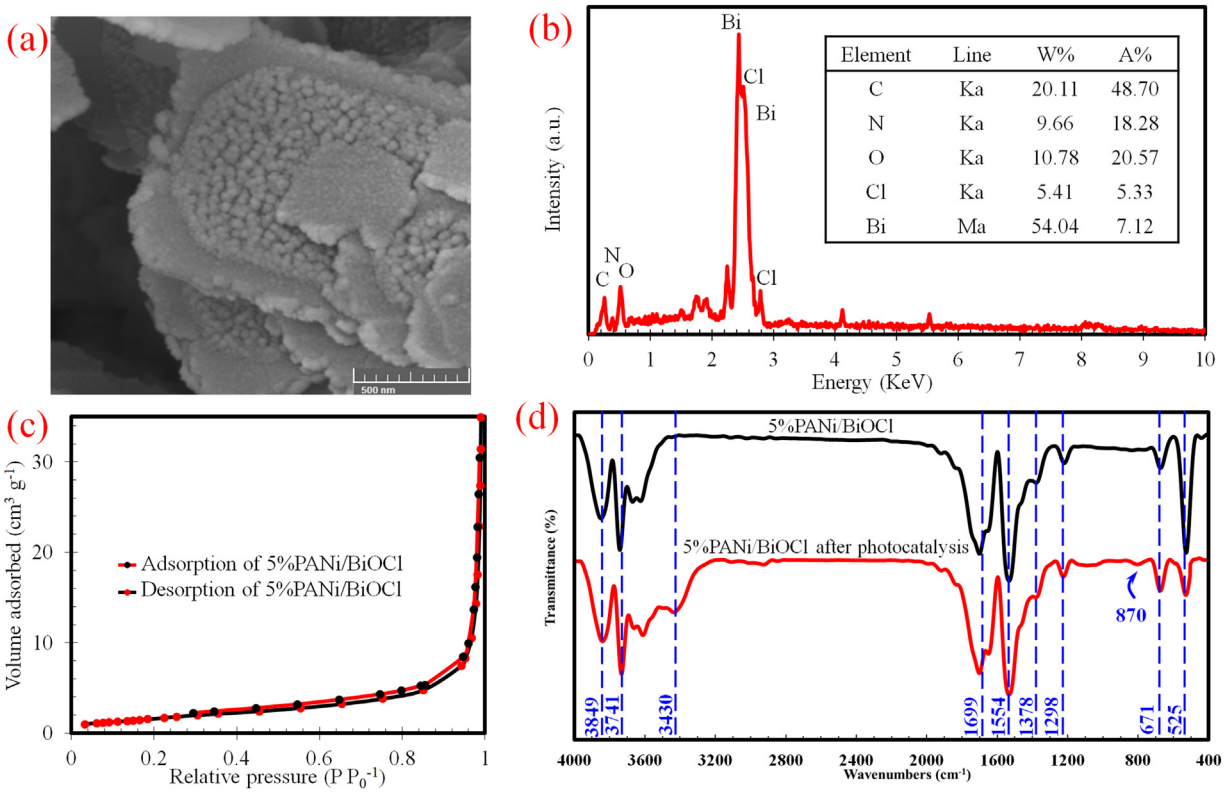

Fig. 7. (a) SEM of 5 wt% PANi/BiOCl nanocomposites after photocatalysis(b) EDX spectra of 5 wt% PANi/BiOCl nanocomposites after photocatalysis (c) N_2 adsorption–desorption of 5 wt% PANi/BiOCl nanocomposites after photocatalysis, (d) FT-IR of 5 wt% PANi/BiOCl nanocomposite before and after photocatalysis.

nanocomposite, the characteristic peaks of PANi at 1554 cm^{-1}, 1378 cm^{-1}, and 1298 cm^{-1} along with the sharp peak of Bi—O are observed, which prove the existence of both PANi and BiOCl in the synthesized nanocomposite. In the 5 wt% PANi/BiOCl after photocatalysis sample, the peak about 3430 cm^{-1}, 870 cm^{-1} and can be attributed to OH with intermolecular hydrogen bond and S—O, respectively[68].

It is important to verify the types of semiconductors by using Mott–Schottky (M–S) measurements, as well as their flat band potentials (V_{fb}) [69]. V_{fb} of the samples can be estimated by extrapolating their linear fits to $C^{-2} = 0$ [70]. As shown in Fig. 8, BiOCl and PANi flat band (FB) potential estimated to −0.69 V (CB of BiOCl) and −1.06 V (LUMO of PANi) to calomel electrode. The vacuum hydrogen electrode was 0.24 V higher than the calomel electrode. So, the CB of BiOCl and LUMO of PANi were −0.82 eV and −0.45 eV. According to the $E_g = VB–CB$, and by considering bandgaps of pure BiOCl, PANi, the VB and HOMO can be estimated 2.65 eV and 2.27 eV for BiOCl and PANi respectively.

The photocatalytic mechanism of prepared 5 wt% PANi/BiOCl photocatalyst is shown in Scheme 2. Because BiOCl could absorb UV–vis region light, it can be reliable that BiOCl can be excited under visible light irradiation. On the other hand, PANi bringing the excited-state electrons of HOMO orbital to LUMO orbital, it can absorb visible light to make π–π* transition. Since the conduction band of BiOCl and π*-orbital of PANi have approximately the same energy levels, with effective chemical bond interaction via in-situ polymerization of PANi on BiOCl surface, the excited electrons of PANi could easily transferred to the BiOCl conduction band and subsequently to the photocatalyst surface for subsequent reaction with water and oxygen to produce hydroxyl and superoxide

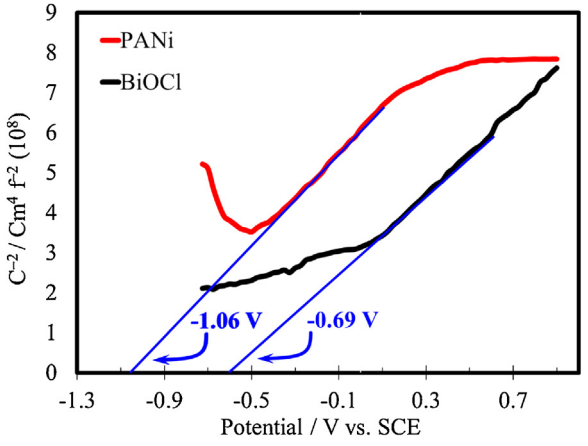

Fig. 8. Mott–Schottky plots of BiOCl and PANi.

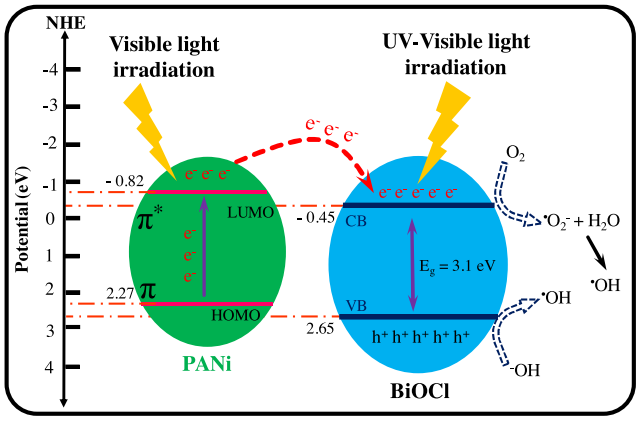

Scheme 2. Photocatalytic degradation mechanism of CR with 5 wt% PANi/BiOCl nanocomposite.

radicals acting as oxidants of CR. Therefore, rapid photogenerated charge separation and relatively slow charge recombination are achieved, which significantly enhances the photocatalytic activity of the 5 wt% PANi/BiOCl nanocomposite.

By using GC–MS analysis, the intermediates and products of photocatalytic degradation of CR were determined. The degradation results are showed in Table S1 for the match factor of mass spectrum higher than 90%. Therefore, compounds were effectively identified. Nevertheless, due to the slight accumulation and limitation associated with the GC–MS method, identification of all intermediates is not possible.

Conclusions

In conclusion, we developed a new approach to synthesis 2D BiOCl sheets decorated by PANi nanoarrays as an efficient visible light driven photocatalyst for the removal of CR. The characterization techniques showed the effective growth and attachment of PANi nanoarrays on 2D BiOCl sheets which enhanced the active surface area and light-absorbing behavior, especially in the visible region. Almost 83.5% of CR at 10 mg L^{-1} was removed by 5 mg of 5 wt% loading of PANi/BiOCl within 60 min were the initial neutral pH (7) remained unchanged. Moreover, with the identification of intermediates, the studied Vis/PANi/BiOCl system was capable of effective CR degradation under determined optimal condition. The in-situ synthesis of PANi nanostructures on 2D BiOCl sheets resulted from effective synergistic effects between two components and considerable photocatalytic activity. With a simple synthesis approach and considerable dye removal ability, the developed PANi/BiOCl photocatalyst can be considered for further environmental remediation applications.

Conflict of interest

There are no conflicts to declare.

Acknowledgments

The authors would like to acknowledge the University of Tabriz for support of this research.

Appendix A. Supplementary data

Supplementary material related to this article can be found, in the online version, at doi:https://doi.org/10.1016/j.jiec.2019.09.012.

References

[1] R. Hassandoost, S.R. Pouran, A. Khataee, Y. Orooji, S.W. Joo, J. Hazard. Mater. 376 (2019) 200.
[2] M. Pirhashemi, A. Habibi-Yangjeh, S. Rahim Pouran, J. Ind. Eng. Chem. 62 (2018) 1.
[3] Y. Tian, W. Li, C. Zhao, Y. Wang, B. Zhang, Q. Zhang, Appl. Catal. B: Environ. 213 (2017) 136.
[4] M.E. Mahmoud, A.E.H. Abdou, A.K. Shehata, H.M.A. Header, E.A. Hamed, J. Ind. Eng. Chem. 57 (2018) 28.
[5] K. Natarajan, H.C. Bajaj, R.J. Tayade, J. Ind. Eng. Chem. 34 (2016) 146.
[6] T. Kamal, S.B. Khan, A.M. Asiri, Cellulose 23 (2016) 1911.
[7] A.H. Pizarro, Catal. Commun. 90 (2017) 100.
[8] A.B. Albadarin, M.N. Collins, M. Naushad, S. Shirazian, G. Walker, C. Mangwandi, Chem. Eng. J. 307 (2017) 264.
[9] A.A. Alqadami, M. Naushad, Z. Alothman, T. Ahamad, J. Environ. Manag. 223 (2018) 29.
[10] R. Molinari, F. Pirillo, M. Falco, V. Loddo, L. Palmisano, Chem. Eng. Process.: Process Intensif. 43 (2004) 1103.
[11] Z. Issaabadi, M. Nasrollahzadeh, S.M. Sajadi, J. Clean. Prod. 142 (2017) 3584.
[12] D. Pathania, G. Sharma, A. Kumar, M. Naushad, S. Kalia, A. Sharma, Z.A. ALOthman, Toxicol. Environ. Chem. 97 (2015) 526.
[13] G. Sharma, M. Naushad, D. Pathania, A. Mittal, G. El-Desoky, Desalin. Water Treat. 54 (2015) 3114.
[14] H. Yao, H. Li, T. Hu, W. Hou, ChemCatChem 10 (2018) 3726.
[15] H.J. Yoon, Y.I. Choi, E.-S. Jang, Y. Sohn, J. Ind. Eng. Chem. 32 (2015) 137.
[16] J. Li, Y. Yu, L. Zhang, Nanoscale 6 (2014) 8473.
[17] H. Zhang, L. Liu, Z. Zhou, RSC Adv. 2 (2012) 9224.
[18] P. Ye, J. Xie, Y. He, L. Zhang, T. Wu, Y. Wu, Mater. Lett. 108 (2013) 168.
[19] J. Xiong, G. Cheng, F. Qin, R. Wang, H. Sun, R. Chen, Chem. Eng. J. 220 (2013) 228.
[20] Y. Xu, D. Lin, X. Liu, Y. Luo, H. Xue, B. Huang, Q. Chen, Q. Qian, ChemCatChem 10 (2018) 2496.
[21] Q. Wang, J. Hui, Y. Huang, Y. Ding, Y. Cai, S. Yin, Z. Li, B. Su, Mater. Sci. Semicond. Process. 17 (2014) 87.
[22] X. Zhang, Z. Ai, F. Jia, L. Zhang, J. Phys. Chem. C 112 (2008) 747.
[23] X. Chang, J. Huang, C. Cheng, Q. Sui, W. Sha, G. Ji, S. Deng, G. Yu, Catal. Commun. 11 (2010) 460.
[24] J. Henle, P. Simon, A. Frenzel, S. Scholz, S. Kaskel, Chem. Mater. 19 (2007) 366.
[25] L. Ye, L. Zan, L. Tian, T. Peng, J. Zhang, Chem. Commun. 47 (2011) 6951.
[26] L. Xu, J. Wang, Environ. Sci. Technol. 46 (2012) 10145.
[27] G. Li, F. Qin, R. Wang, S. Xiao, H. Sun, R. Chen, J. Colloid Interface Sci. 409 (2013) 43.
[28] W. Fan, C. Zhang, W.W. Tjiu, K.P. Pramoda, C. He, T. Liu, ACS Appl. Mater. Interfaces 5 (2013) 3382.
[29] W. Li, S.-a. He, W. Xu, J. Li, X.-c. Wang, Electrochim. Acta 283 (2018) 727.
[30] P.-Q. Wang, Y. Bai, J.-Y. Liu, Z. Fan, Y.-Q. Hu, Micro Nano Lett. 7 (2012) 876.
[31] M. Amini, R. Hassandoost, M. Bagherzadeh, S. Gautam, K.H. Chae, Catal. Commun. 85 (2016) 13.
[32] J. Cao, B. Xu, H. Lin, B. Luo, S. Chen, Catal. Commun. 26 (2012) 204–208.
[33] L. Zhang, W. Wang, S. Sun, Y. Sun, E. Gao, J. Xu, Appl. Catal. B: Environ. 132 (2013) 315.
[34] F. Gao, D. Zeng, Q. Huang, S. Tian, C. Xie, PCCP 14 (2012) 10572.
[35] L. Ye, K. Deng, F. Xu, L. Tian, T. Peng, L. Zan, PCCP 14 (2012) 82.
[36] M. Guan, C. Xiao, J. Zhang, S. Fan, R. An, Q. Cheng, J. Xie, M. Zhou, B. Ye, Y. Xie, J. Am. Chem. Soc. 135 (2013) 10411.
[37] M.J. Chatterjee, S.T. Ahamed, M. Mitra, C. Kulsi, A. Mondal, D. Banerjee, Appl. Surf. Sci. 470 (2019) 472.
[38] Y. Xu, Y. Ma, H. Ji, S. Huang, M. Xie, Y. Zhao, H. Xu, H. Li, J. Colloid Interface Sci. 537 (2019) 101.
[39] Q. Wang, J. Hui, J. Li, Y. Cai, S. Yin, F. Wang, B. Su, Appl. Surf. Sci. 283 (2013) 577.
[40] R. Tanwar, B. Kaur, U.K. Mandal, Appl. Catal. B: Environ. 211 (2017) 305.
[41] R. Tanwar, S. Kumar, U.K. Mandal, J. Photochem. Photobiol. A: Chem. 333 (2017) 105.
[42] Y. Mi, L. Wen, Z. Wang, D. Cao, R. Xu, Y. Fang, Y. Zhou, Y. Lei, Nano Energy 30 (2016) 109.
[43] A. Khataee, R. Hassandoost, S. Rahim Pouran, Ultrason. Sonochem. 41 (2018) 626.
[44] S.Y. Chai, Y.J. Kim, M.H. Jung, A.K. Chakraborty, D. Jung, W.I. Lee, J. Catal. 262 (2009) 144.
[45] Y. Lei, G. Wang, S. Song, W. Fan, H. Zhang, CrystEngComm 11 (2009) 1857.
[46] Y. Tian, C.F. Guo, Y. Guo, Q. Wang, Q. Liu, Appl. Surf. Sci. 258 (2012) 1949.
[47] L. Liu, L. Ding, Y. Liu, W. An, S. Lin, Y. Liang, W. Cui, Appl. Catal. B: Environ. 201 (2017) 92.
[48] Z. Wang, X. Peng, C. Huang, X. Chen, W. Dai, X. Fu, Appl. Catal. B: Environ. 219 (2017) 379.
[49] F. Zhang, T. Ding, Y. Zhang, Z. Yang, H. Xue, Mater. Lett. 192 (2017) 149.
[50] R. Tanwar, B. Kaur, U. Kumar Mandal, Appl. Catal. B: Environ. 211 (2017) 305.
[51] S. Shamaila, A.K.L. Sajjad, F. Chen, J. Zhang, J. Colloid Interface Sci. 356 (2011) 465.
[52] A.G. Tabrizi, N. Arsalani, A. Mohammadi, L.S. Ghadimi, I. Ahadzadeh, H. Namazi, Electrochim. Acta 265 (2018) 379.
[53] A.G. Tabrizi, N. Arsalani, Z. Naghshbandi, L.S. Ghadimi, A. Mohammadi, Int. J. Hydrogen Energy 43 (2018) 12200.
[54] A.G. Tabrizi, N. Arsalani, A. Mohammadi, L.S. Ghadimi, I. Ahadzadeh, J. Colloid Interface Sci. 531 (2018) 369.
[55] J. Di, J. Xia, S. Yin, H. Xu, L. Xu, Y. Xu, M. He, H. Li, RSC Adv. 4 (2014) 14281.
[56] H. Gnayem, Y. Sasson, J. Phys. Chem. C 119 (2015) 19201.
[57] M. Naushad, T. Ahamad, B.M. Al-Maswari, A.A. Alqadami, S.M. Alshehri, Chem. Eng. J. 330 (2017) 1351.
[58] M. Naushad, T. Ahamad, G. Sharma, H. Ala'a, A.B. Albadarin, M.M. Alam, Z.A. ALOthman, S.M. Alshehri, A.A. Ghfar, Chem. Eng. J. 300 (2016) 306.
[59] J. Xia, L. Xu, J. Zhang, S. Yin, H. Li, H. Xu, J. Di, CrystEngComm 15 (2013) 10132.
[60] D. Zhao, X. Yang, C. Chen, X. Wang, J. Colloid Interface Sci. 398 (2013) 234.
[61] S.H. Piao, M. Bhaumik, A. Maity, H.J. Choi, J. Mater. Chem. C 3 (2015) 1861.
[62] D. Zhao, G. Sheng, C. Chen, X. Wang, Appl. Catal. B: Environ. 111–112 (2012) 303.
[63] H. Cheng, B. Huang, X. Qin, X. Zhang, Y. Dai, Chem. Commun. (Camb) 48 (2012) 97.
[64] B. Krishnakumar, M. Swaminathan, Spectrochim. Acta A: Mol. Biomol. Spectrosc. 81 (2011) 739.
[65] Z.A. Al-Othman, R. Ali, M. Naushad, Chem. Eng. J. 184 (2012) 238.
[66] C. Vidya, C. Manjunatha, M. Chandraprabha, M. Rajshekar, A.R. MAL, J. Environ. Chem. Eng. 5 (2017) 3172.
[67] L. Chen, S. Feng, D. Zhao, S. Chen, F. Li, C. Chen, J. Colloid Interface Sci. 490 (2017) 197.
[68] N.A. Abdelwahab, F.M. Helaly, J. Ind. Eng. Chem. 50 (2017) 162.
[69] X. Xu, R. Liu, Y. Cui, X. Liang, C. Lei, S. Meng, Y. Ma, Z. Lei, Z. Yang, Appl. Catal. B: Environ. 210 (2017) 484.
[70] H. Liu, D. Chen, Z. Wang, H. Jing, R. Zhang, Appl. Catal. B: Environ. 203 (2017) 300.